

3-DIMENSIONAL CELLULAR AUTOMATA SIMULATION OF GRAIN STRUCTURE IN METAL ADDITIVE MANUFACTURING PROCESSES

Xuxiao Li and Wenda Tan

Department of Mechanical Engineering, The University of Utah, Salt Lake City, UT 84112

Abstract

Distinct grain structures have been observed in Metal Additive Manufacturing (MAM) processes. These grain structures feature columnar grains which occasionally mix with equiaxed grains. The occurrence of these grain structures is not yet fully understood. In this work, direct laser deposition process is studied as a typical MAM process. A finite volume model is first implemented to obtain the thermal history. Next, the thermal history is fed into a Cellular Automata (CA) model to simulate the epitaxial and competitive growth through which the columnar grains are formed. Nucleation is included in the model to predict the generation of equiaxed grains, and is characterized by two nucleation parameters, the nucleation density and the critical undercooling. The simulation results show that both the nucleation parameters and process parameters can significantly affect the grain structure. The simulated grain structures examined on different planes can be significantly different, revealing the complexity of the 3-dimensional grain structures in MAM processes.

1. Introduction

Metal additive manufacturing (MAM) systems are categorized by [1] into three general categories: the powder bed system, the powder feed system, and the wire feed system. Despite a fair diversity in each of these systems, a typical MAM process can be described as follows: the metal material is constantly fed to a moving energy source (electron beam or laser); the energy source melts the metal, and the metal solidifies to become the built part once the energy source moves away. Then the process is repeated in a layer-by-layer fashion in which complex 3-Dimensional (3D) geometry can be achieved. So far MAM processes have been studied intensively with a wide variety of metal alloys such as stainless steel 316L, aluminum alloy AlSi10Mg, titanium alloy Ti6Al4V, and nickel alloy IN718.

Certain distinct grain structure features have been observed in MAM which actually apply to different metal alloys and MAM systems. Columnar grains (grains having large aspect ratio) are almost always observed. The size of columnar grains can depend on the power of the energy source [2]. The orientation along which columnar grains grow can be changed by adjusting the scanning direction of the energy source [3]. Equiaxed grains (grains having small aspect ratio) are also observed in MAM, usually at the surface of the built [4, 5], but can be dispersed among columnar grains [6], “sandwiched” between two layers of columnar grains [2], or located specifically on the border of the molten pool [7]. Strong grain texture is found from elongated columnar grains, while equiaxed grains tend to reduce grain texture [6-10]. Different grain structures can cause significant variance and anisotropy in the mechanical property of the built part [8]. Therefore, it is very important to understand the mechanism of the occurrence of these grain structures in order to control the built quality and to even tailor desired grain structures [10].

In literature, there exist widely accepted explanations for the occurrence of columnar and equiaxed grains, such as that found in [11]. The columnar grains are considered to be caused by an epitaxial growth mechanism [12] in which all the existing grains keep growing along one “easy-growth” direction ($\langle 100 \rangle$ direction for body-centered-cubic and face-centered-cubic metals [12]). Since only one direction is favored for grain growth, grains can be “stretched” and become columnar. The occurrence of equiaxed grains is attributed to the heterogeneous nucleation ahead of the Solidification Front (SF) [13]. If the total volume of the equiaxed grains ahead of the SF is large enough, columnar grains can be blocked by the equiaxed grains (Columnar-to-Equiaxed Transition, or CET). Depending on the local temperature gradient, G , and the SF velocity V , the grain structure can be either columnar or equiaxed [14, 15].

Simulation works [16-21] have been dedicated to quantifying the above mechanisms of grain structure evolution. Among them, Cellular Automata (CA) method has been successfully implemented to model the epitaxial growth of columnar grains. Ref. [16] reveals that the orientation toward which the columnar grain grows is complexly determined by the local G on the SF. Ref. [17] shows a gradual enlargement of grain size in the building direction due to the competitive growth of the columnar grains. By incorporating a classical nucleation model to CA method, the occurrence of equiaxed grains is also captured [17, 21]. The evolution of grain structure is highly coupled with the temperature condition around the molten pool, $T(x, y, z, t)$, also referred as the thermal history, which actually determines the local G and V . However, modeling thermal history $T(x, y, z, t)$ is a very challenging task due to the complication caused by the fluid flow in the molten pool [22] as well as the geometry of metal powders [23]. It is also found that the gas flow will influence the size of the molten pool [24]. Therefore, different levels of simplifications are assumed in literature such as ignoring the fluid flow and treating the metal powder as a homogeneous continuum, as reviewed in [25].

In this work, the laser direct deposition process is studied as a typical MAM process. A temperature simulation based on heat conduction is first implemented to obtain the thermal history. Then a 3D CA model combined with a nucleation model is used to capture the epitaxial growth of columnar grains as well as the occurrence of equiaxed grains. Compared to existing works, this work features a detailed discussion about the nucleation in MAM, as it turns out that nucleation conditions can significantly affect the grain structure. This work also reveals the complexity of the 3D grain structure in MAM while most of the existing work is limited to 2D. Parametric studies of laser power and scanning speed are conducted to demonstrate their effects on grain structure.

2. Model description

2.1 Temperature modeling

The temperature modeling methodology is adapted from a finite volume model for laser direct deposition [26] where a Cartesian grid and a level-set formulation are used to capture the metal-gas interface. The level-set equation is written as (Equation 1):

$$\frac{\partial \psi}{\partial t} + F_p |\nabla \psi| = 0, \quad (1)$$

where ψ is the level-set function, defined as the “signed distance” to the metal-gas interface [27]. ψ is defined positive on the gas region, negative on the metal region, and as zero on the metal-gas interface, as illustrated in Figure 1. F_p is the interface growth velocity due to powder addition, which determines the evolution of ψ (Figure 1).

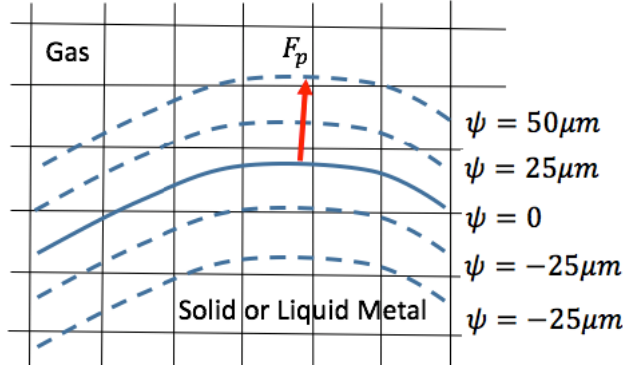


Figure 1: Illustration of the level-set function ψ and the interface growth velocity F_p .

By ignoring fluid flow, the temperature is solved only from the heat conduction equation, which is formulated in a conservative form (Equation 2):

$$\frac{\partial(\rho e)}{\partial t} = k \nabla^2 T + \dot{S}, \quad (2)$$

where ρ is the density, e is the specific internal energy, k is the thermal conductivity, T is the temperature, and \dot{S} is the source term of the energy conservation equation. The material properties, ρ , e , and k are defined according to the local phase (solid metal, liquid metal, mushy metal or gas). The material studied in this work is stainless steel (SS) 316L for the metal phase and argon for the gas phase, the properties of which are given in Table 1. The source term \dot{S} is located on the metal-gas interface and is composed of several parts (Equation 3):

$$\dot{S} = \dot{S}_{laser} + \dot{S}_{conv} + \dot{S}_{rad}. \quad (3)$$

The four terms on the RHS of Equation 3 represent the energy source from the laser absorption as well as the energy loss from convection and radiation, respectively. \dot{S}_{laser} is treated as a Gaussian distributed surface source term. Further details about Equation 1-3 is referred to [26, 28].

Table 1: Material properties of stainless steel 316L and argon.

Property	Stainless steel 316L		Argon
	Solid	Liquid	
Density (kg m ⁻³)	8000	8000	1.784
Specific heat (J kg ⁻¹ K ⁻¹)	500	500	312
Thermal conductivity (W m ⁻¹ K ⁻¹)	19.2	209	0.44
Liquidus temperature (K)		1673	
Solidus temperature (K)		1648	
Melting Latent heat (J kg ⁻¹)		250000	

The Cartesian grid used for the temperature modeling is shown in Figure 2. A non-uniform grid (covering both gas and metal phases) is applied. In this work, +Y is the vertical (building) direction and the laser scans in the XZ plane. The laser scans only in the fine mesh region (the zoom-in region in Figure 2, with the mesh size being 25 μm) at the center of the calculation domain to guarantee the accuracy of the thermal history near the molten pool.

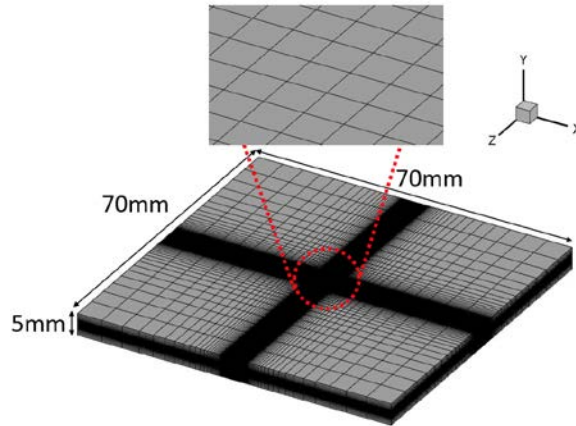


Figure 2: The Cartesian grid used for temperature simulations.

2.2 Grain structure modeling

The thermal history obtained from temperature model is then used as the input for the grain structure simulations. A 3D CA model based on a decentered square method is used to model the grain growth. A detailed description of this model can be referred to [28-30]. A uniform Cartesian grid is used for the CA model, with a mesh size of 3 μm , which is about one tenth of the typical size of substrate grains ($\sim 30 \mu\text{m}$). The substrate grains are equiaxed grains randomly generated before a simulation starts. The local growth velocity of each grain is assumed to be a function of the local undercooling, referred as the “grain growth kinetics” (Equation 4):

$$V_g = a(\Delta T)^3 + b(\Delta T)^2 + c\Delta T + d, \quad (4)$$

$$a = 1.091 \times 10^{-5}, b = -2.034 \times 10^{-4}, c = 2.740 \times 10^{-3}, d = 1.151 \times 10^{-4}$$

where V_g is the local growth velocity (unit: m/s); ΔT is the local undercooling defined as $\Delta T = T_m - T$ (unit: K), where T_m is the metal liquidus temperature and T is the local temperature. The grain growth kinetics (Equation 4) is obtained by a polynomial interpolation from the results in [29], as is the common practice in CA method [30].

In the current model, there are two nucleation mechanisms based on which grains start their growth: the epitaxial nucleation on the SF and the heterogeneous nucleation ahead of the SF. On the SF, nucleation takes place by attaching the liquid atoms onto the partially melted grains on the fusion line such that the attached atoms are arranged in the same crystal orientation as those of the partially melted grains. This nucleation mechanism is referred as the epitaxial nucleation and is assumed to occur immediately once the local temperature on the SF drops below the liquidus temperature. Epitaxial growth refers to the grain growth initiated by epitaxial nucleation. Ahead

of the SF, heterogeneous nucleation can take place at “substrates” such as the impurities in the liquid metal, where the activation energy of nucleation is reduced. The liquid atoms are then attached to the substrates and are assumed to be arranged in a random crystal orientation. This nucleation mechanism is referred as heterogeneous nucleation in this work. It is noted that in epitaxial nucleation the growing grains only “inherit” existing crystal orientations while in heterogeneous nucleation the growing grains have new orientations.

In this work, heterogeneous nucleation is modeled using the continuous nucleation model [31]. In this model, the nucleation rate I and the number of nuclei N are continuous functions of the undercooling, as shown in Figure 3. At a critical undercooling the number of nuclei changes rapidly from zero to the maximum value N_0 . The nucleation rate exhibits a peak at a critical undercooling while maintains zero when the undercooling being too large or too small. The nucleation rate, as a function of undercooling, can be considered as a Gaussian distribution, characterized by the mean undercooling $\Delta T_{N,mean}$, and the standard deviation $\Delta T_{N,sig}$, which can be determined by experimental observations [32].

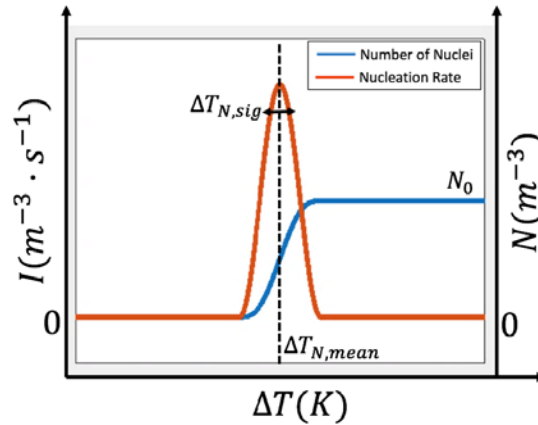


Figure 3: Illustration of continuous nucleation model.

The method in [33] is used to implement the continuous nucleation model. The three parameters N_0 , $\Delta T_{N,mean}$, and $\Delta T_{N,sig}$ illustrated in Figure 3 are first determined for the nucleation. Then according to N_0 random cells in the CA model are selected as potential locations for nucleation to occur; for each potential nucleation location, a critical undercooling is assigned based on the Gaussian distribution characterized by $\Delta T_{N,mean}$ and $\Delta T_{N,sig}$. When a potential nucleation cell is still liquid and the local undercooling is larger than the assigned critical nucleation undercooling of the cell, this cell will change from liquid to a nucleus, from which a new grain starts growing. The grain growth after epitaxial nucleation and heterogeneous nucleation is treated in the same way based on the decenter square method and the growth kinetics in Equation 4.

3. Results and Discussion

3.1 Thermal history

A typical single-pass simulation result (scanning direction +X) is shown in Figure 4. Figure 4a shows a 3D view of the zero-level-set surface flooded by the temperature. The zero-level-set surface is the metal-gas interface which indicates the geometry of the built track (length: 3.5mm).

Figure 4b-d show a three-view drawing of the region near the molten pool to better demonstrate the molten pool geometry (marked by solid black line). From the top view (Figure 4b) the molten pool is of the shape of a teardrop elongated along the X direction, as similar to those observed in welding processes [12]. Some geometric definitions of the molten pool referred in this work are given as follows: the point with the highest temperature on the zero-level-set isosurface is referred as the laser center (the orange circle), and the XY plane that contains the laser center is referred as the center plane (the red dashed line). The “tail” of the molten pool (the blue circle) is defined as the tip of the teardrop on the top view. The “bottom” of the molten pool (the blue triangle) is the deepest position of the molten pool. The “fusion surface”, marked by the yellow dashed line, is defined as the part of the molten pool surface that will instantly solidify (temperature dropping below the liquidus temperature) when laser further scans in the +X direction.

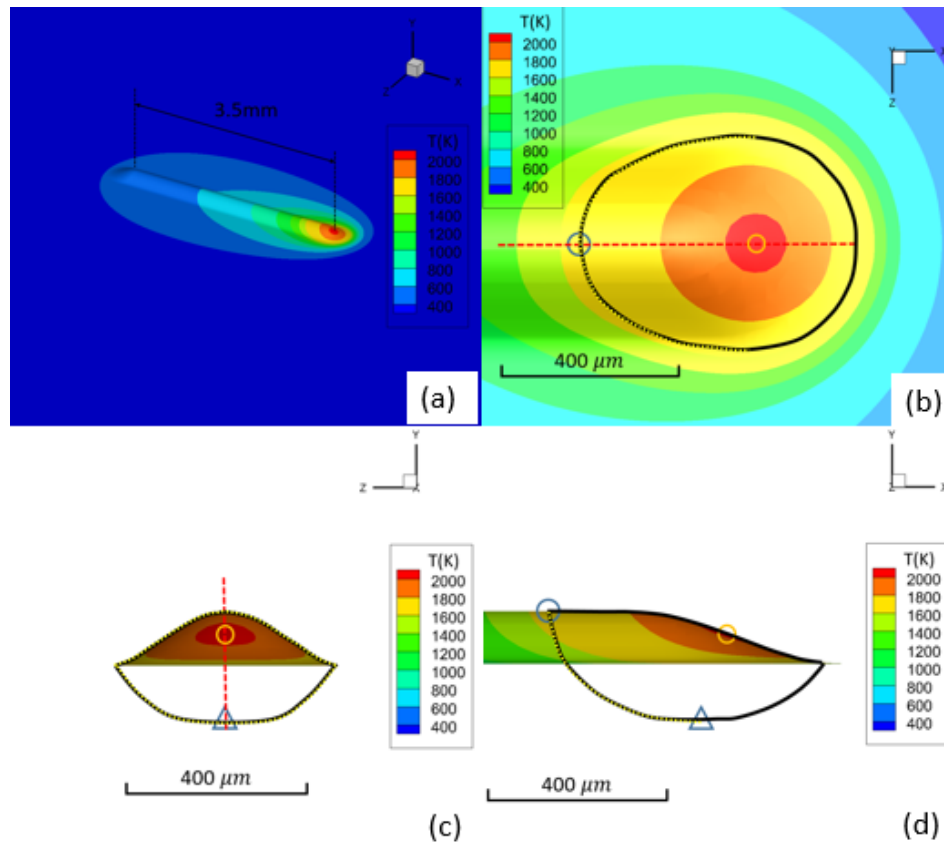


Figure 4: Typical single-pass temperature simulation results. (a) is the 3D view of zero-level-set isosurface (metal-gas interface) flooded with temperature distribution. (b)-(d) are the top view, side view and front view of the molten pool (boundary marked by black solid line). The orange circle marks the laser center; the red dashed line marks the center plane; the yellow dotted line marks the fusion surface; the blue circle marks the molten pool tail; the blue triangle marks the molten pool bottom.

Multi-pass simulation is implemented by applying the energy source (\dot{S}_{laser} and \dot{S}_{add} in Equation 3) and the powder addition (F_p in Equation 1) to different locations at different times according to the laser speed and scanning pattern. Shown in Figure 5 is an example in which the laser scans with a zigzag pattern along the X direction. This process can be repeated for multi-pass, multi-layer simulations.

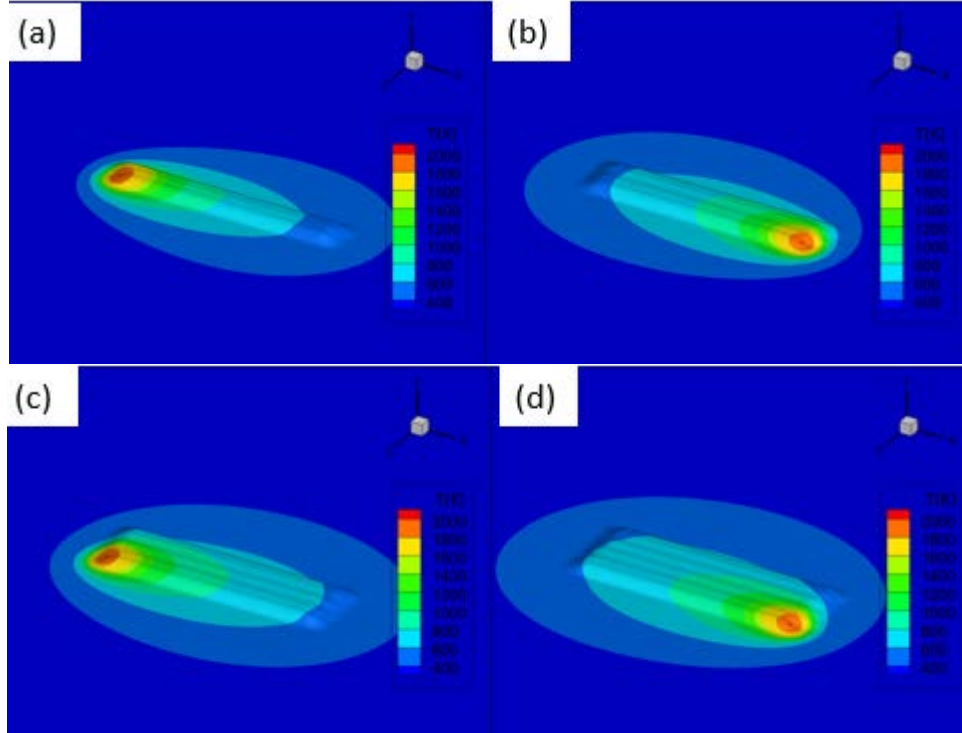


Figure 5: 3D view of zero-level-set isosurface flooded with temperature distribution in multi-pass simulations. The laser scans in a zigzag way along the X direction. (a)-(d) show the simulation results at the end of the second, third, fourth and fifth pass. The simulation result at the end of the first track is shown in Figure 4a.

3.2 Effects of maximum nucleation density and mean critical undercooling

A series of single-pass simulations (scanning direction +X) are carried out to investigate the effects of the maximum nucleation density N_0 and the mean critical undercooling $\Delta T_{N,mean}$. Due to a lack of experimental calibration of N_0 and $\Delta T_{N,mean}$, a range of N_0 and $\Delta T_{N,mean}$ have been tested and they are found to have a significant influence on the grain structure. The laser power P and scanning velocity V_{laser} used in this section are 200 W and 26 mm/s.

In order to better rationalize the simulation results, Hunt's analytical model [13] is used to compare with the simulation results. In Hunt's model, G-V maps are analytically computed to show the (G, V) combinations that lead to grain structures of either completely columnar, completely equiaxed, or "mixed" with columnar and equiaxed grains, as shown in Figure 5a. The G-V maps discussed in this work are all in logarithm with unit conventions of K/m for G and m/s for V . It can be seen in Figure 6a that larger G and smaller V tend to cause columnar grains while smaller G and larger V tend to cause equiaxed grains.

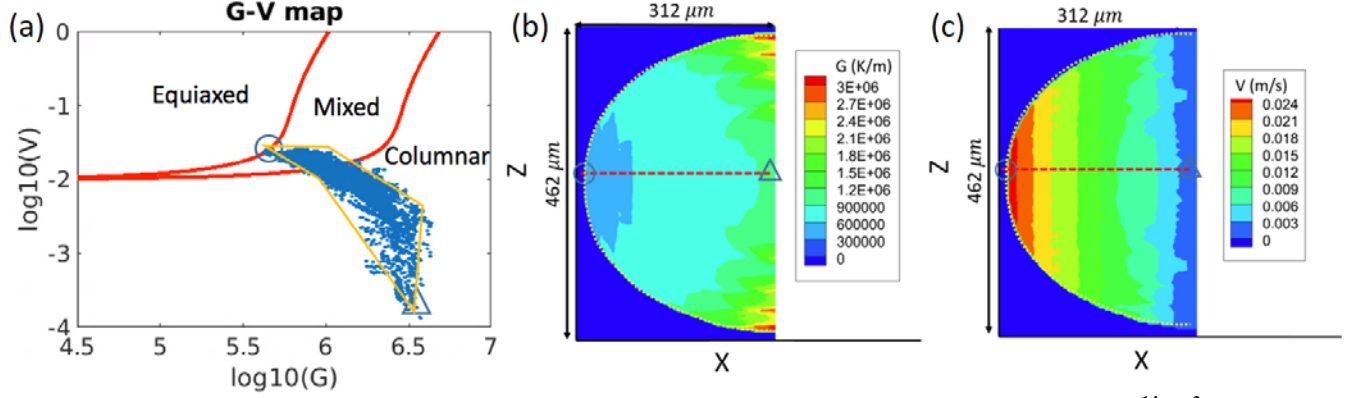


Figure 6: Analysis of (G, V) condition. (a) is the G - V map calculated from Hunt's model with N_0 of 10^{14} m^{-3} and $\Delta T_{N,mean}$ of 5 K. The red curves demarcate the (G, V) combinations that lead to columnar, equiaxed and mixed grain structures. The blue dots are the calculated (G, V) on the fusion surface shown in (b) and (c). The orange polygon marks the region covered by the blue dots. The blue circle and triangle indicate the (G, V) at the tail and bottom of the molten pool. (b) and (c) are the G and V distributions on the fusion surface observed from top view. The red dashed line marks the center plane, the blue circle marks the molten pool tail, and the blue triangle marks the molten pool bottom.

The temperature gradient G and the SF velocity V on the fusion surface are considered along the normal directions of the fusion surface. Their value can be computed from the thermal history by (Equation 5):

$$G_{fs} = \sqrt{\left(\frac{\partial T}{\partial x}\right)^2 + \left(\frac{\partial T}{\partial y}\right)^2 + \left(\frac{\partial T}{\partial z}\right)^2}, \quad (5a)$$

$$V_{fs} = V_{laser} \cos\theta, \quad (5b)$$

$$\cos\theta = ((\partial T / \partial x)) / G_{fs}, \quad (5c)$$

where the subscript “fs” stands for fusion surface. In Equation 5b, θ is the angle between the laser scanning direction (+X) and the local normal direction of the fusion surface. Figure 6b and 6c plot the distributions of G and V on the fusion surface from a top view. It is observed that along the center plane (red dashed line), the smallest G and largest V are found at the tail of the molten pool (blue circle), while the largest G and the smallest V are found at the bottom (blue triangle). Assuming that the normal directions of the fusion surface represent the easy growth directions of grain, it is expected that the equiaxed grains tend to occur at the tail and columnar grains tend to dominate at the bottom. This trend is also demonstrated in Figure 6a as the blue circle (tail) already reaches the completely equiaxed region while the blue triangle (bottom) stays in the completely columnar region.

Now the effects of N_0 on the grain structure are investigated. N_0 is varied as 10^{13} m^{-3} , 10^{14} m^{-3} and 10^{15} m^{-3} while $\Delta T_{N,mean}$ is kept as 5 K. In this work, the simulated grain structure on a certain plane is represented by inverse pole figure (IPF) orientation map in which the “projection direction” (the direction perpendicular to the plane under examination) is mapped to the crystal frames. The color key of the IPF mapping used in this work is shown in Figure 7. The simulated grain structure of the center plane from these single-pass simulations is shown in Figure 8a-c. One can observe that the number of equiaxed grains increases as N_0 increases. There are almost no equiaxed grains visible in Figure 8a; columnar grains grow epitaxially from the substrate (the black

dashed line) toward the laser scanning direction (SD). Equiaxed grains are found interspersed among the dominating columnar grains when N_0 is 10^{14} m^{-3} (Figure 8b). When N_0 is as large as 10^{15} m^{-3} (Figure 8c), the equiaxed grains block the columnar grains which grow epitaxially from the substrate; a CET can be clearly observed. Figure 8d shows the G-V map calculated based on Hunt's model with different N_0 values, and the (G, V) condition on the fusion surface is shown again with the orange polygon. It confirms the results in Figure 8a-c: when N_0 is 10^{13} m^{-3} , the fusion surface (G, V) barely enters the mixed grain region; in contrast when N_0 is 10^{15} m^{-3} , a significantly portion of (G, V) is in the mixed grain region and some is in the completely equiaxed region.

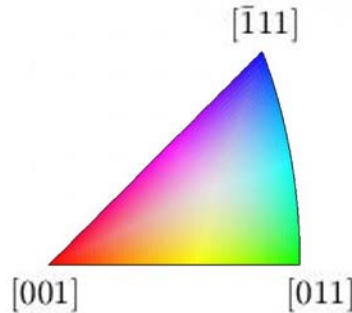


Figure 7: The color key for the inverse pole figure orientation mapping.

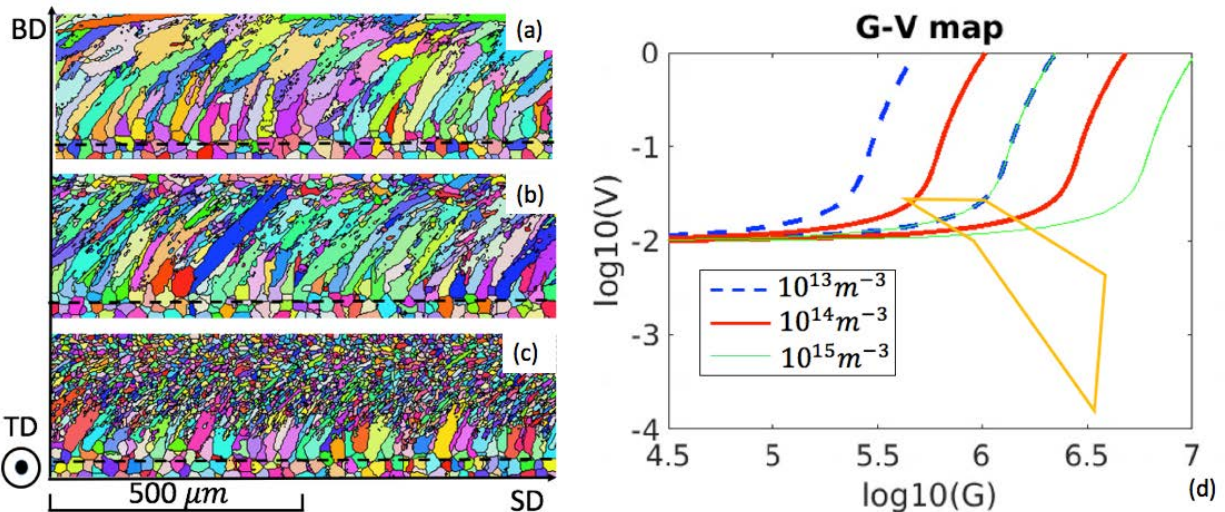


Figure 8: The effects of N_0 on grain structure. $\Delta T_{N,mean}$ is kept as 5 K. (a)-(c) are the grain structures on the center plane with values of N_0 being 10^{13} m^{-3} , 10^{14} m^{-3} and 10^{15} m^{-3} . The black dashed line indicates the location of fusion line. (d) is the G-V map obtained with different values of N_0 ; the orange polygon stands for the (G, V) on the fusion surface.

The effects of $\Delta T_{N,mean}$ is studied next. $\Delta T_{N,mean}$ is varied as 0 K, 5 K, and 10 K while N_0 is fixed as 10^{14} m^{-3} . The simulated grain structure on the center plane and the G-V map is shown in Figure 9. It is observed in Figure 9a-c that a larger $\Delta T_{N,mean}$ causes less equiaxed grain and correspondingly more columnar grains. This point is confirmed in Figure 9d as a decreasing portion of the (G, V) polygon will be covered by the mixed or equiaxed region as $\Delta T_{N,mean}$ increases.

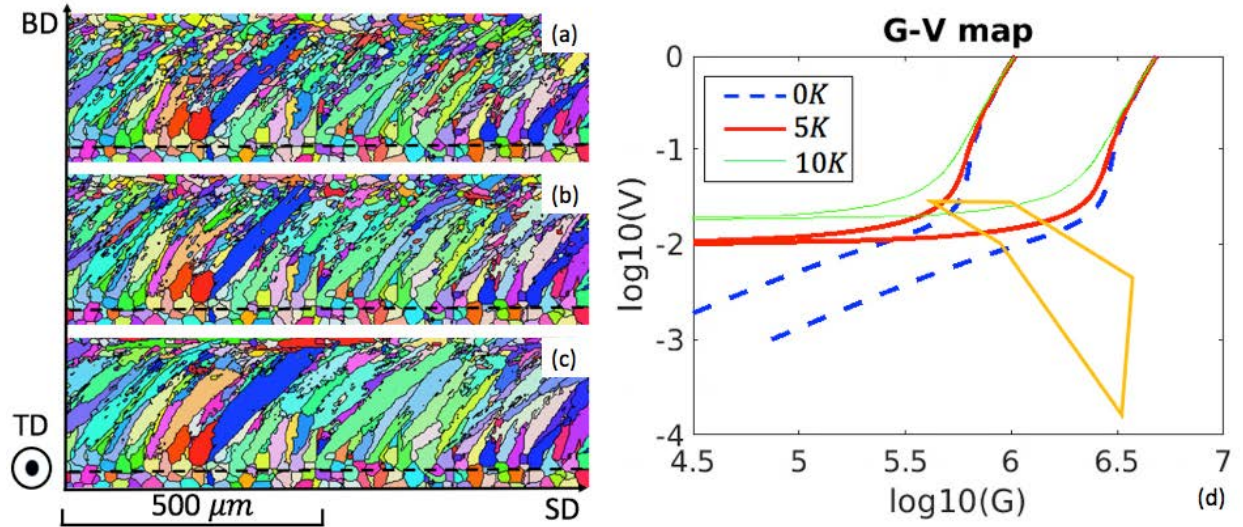


Figure 9: The effects of $\Delta T_{N,mean}$ on grain structure. N_0 is kept as 10^{14} m^{-3} . (a)-(c) are the grain structures on the center plane with the values of $\Delta T_{N,mean}$ being 0 K, 5 K and 10 K. The black dashed line indicates the location of fusion line. (d) is the G-V map obtained with different values of $\Delta T_{N,mean}$; the orange polygon stands for the (G, V) on the fusion surface.

It is concluded through these parametric studies that both large $\Delta T_{N,mean}$ and small N_0 will encourage the domination of columnar grain, while small $\Delta T_{N,mean}$ and N_0 will favor the occurrence of equiaxed grain.

3.3 Effects of laser power and scanning velocity

The effects of laser power P and scanning velocity V_{laser} are studied by carrying out single-pass simulations using the three sets of (P, V_{laser}) in Table 2. N_0 is fixed as 10^{14} m^{-3} and $\Delta T_{N,mean}$ as 5 K. The simulated grain structure on the center plane and the G-V map is shown in Figure 10.

Table 2: Process parameters used in section 3.3

Set	Laser power (W)	Scanning velocity (mm/s)
1	200	26
2	400	26
3	200	8.8

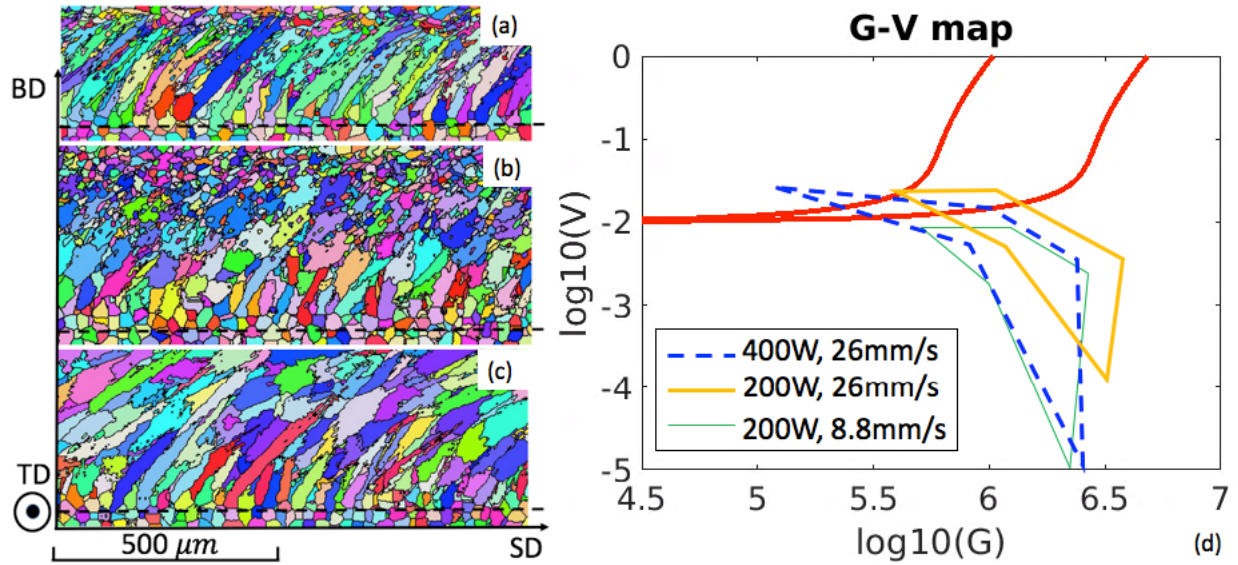


Figure 10: The effects of P and V_{laser} on grain structure. N_0 is kept as 10^{14} m^{-3} and $\Delta T_{N,mean}$ as 5 K. (a)-(c) are the grain structures on the center plane with different the values of P and V_{laser} : (a) for $P = 200 \text{ W}$, $V_{laser} = 26 \text{ mm/s}$; (b) for $P = 400 \text{ W}$, $V_{laser} = 26 \text{ mm/s}$; (c) for $P = 200 \text{ W}$, $V_{laser} = 8.8 \text{ mm/s}$. The black dashed line indicates the location of fusion line. (d) is the G-V map obtained with $N_0 = 10^{14} \text{ m}^{-3}$ and $\Delta T_{N,mean} = 5 \text{ K}$; the three polygons of orange, blue and green color stand for the (G, V) on the fusion surface computed with different values of P and V_{laser} .

The effects of P can be seen by comparing Figure 10a and 10b in which V_{laser} is kept at 26mm/s while P is varied from 200 W (Figure 10a) to 400 W (Figure 10b). It is observed that increasing the laser power will encourage the occurrence of equiaxed grain, as columnar grain still dominates in Figure 10a but a CET is clearly observed in Figure 10b. This can be explained by comparing the G-V polygons (blue and orange) of the two cases in Figure 10d. These two regions are comparable in terms of the largest V , as the same V_{laser} is applied in these two cases. However, a higher power (blue polygon) gives a much smaller minimum G on the fusion surface, which encourages the occurrence of equiaxed grain especially at the tail region; therefore, a CET is observed in Figure 10b.

The effects of V_{laser} can be seen by comparing Figure 10a and 10c, as P is fixed as 200 W while V_{laser} is varied from 26 mm/s (Figure 10a) to 8.8 mm/s (Figure 10c). Reducing the scanning velocity tends to eliminate the occurrence of equiaxed grains, as in Figure 10a interspersed equiaxed grains are still visible while in Figure 10c grains are completely columnar. Again, this point can be explained in Figure 10d by comparing the green and orange polygons. The two polygons cover a common range of G , but the green polygon has a smaller V than the orange one due to smaller V_{laser} . Therefore, the green polygon is entirely within the completely columnar region, leading to the completely columnar grain structure in Figure 10c.

It has been demonstrated through this series of simulations that the process parameters can significantly change the grain structuring via altering the local (G, V) condition. It is foreseeable that an effective simulation can help make “a priori selection of process parameters for tailored microstructure [34]” and (partially) replace the trial-and-error tests for optimization.

3.4 Preliminary results for multi-pass multi-layer simulation

Preliminary multi-pass multi-layer simulations are carried out to explore possible grain structures under different N_0 and $\Delta T_{N,mean}$. The process parameters used in this section are: $P = 200$ W, $V_{laser} = 26$ mm/s, and a hatch spacing of $250 \mu\text{m}$. $(N_0, \Delta T_{N,mean})$ combinations used in this section are listed in Table 3. The simulation consists of eight layers with a thickness of $200 \mu\text{m}$ for each layer, and there are six tracks in every layer. The scanning strategy is illustrated in Figure 11; the laser scans in the X direction in a zigzag pattern within each layer (the red arrows) and the scanning direction changes by 180° between two layers. In this work, the XY planes (such as the green plane in Figure 11) are referred as longitudinal sections and the YZ planes (such as the yellow plane in Figure 11) are referred as cross sections.

Table 3: Nucleation parameters for section 3.4.

Case	N_0 (m^{-3})	$\Delta T_{N,mean}$ (K)
1	10^{13}	10
2	10^{14}	0
3	10^{14}	5
4	10^{15}	0

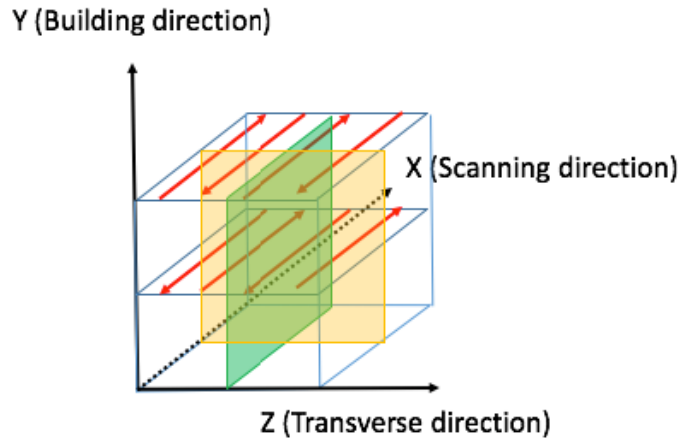


Figure 11: The scanning strategy used in section 3.4.

First, the grain structures on the center plane of the third track are examined (the grain structures are repeatable for the center planes of different tracks), as shown in Figure 12. It is seen that as N_0 increases or $\Delta T_{N,mean}$ decreases from Figure 12a-d, equiaxed grains become increasingly dominant, which is also confirmed in Table 4 with the average aspect ratio of grains decreasing from Figure 12a-d. In Figure 12a-c where large columnar grains are visible, it can be observed that the columnar grains will grow toward the laser scanning direction. Since the laser switches the scanning direction between two layers, the growing direction of columnar grains also switches between two layers. In Figure 12a where the N_0 and $\Delta T_{N,mean}$ favors columnar grains the most ($N_0 = 10^{13} \text{m}^{-3}$, $\Delta T_N = 10\text{K}$) the grain structure is completely columnar; the grains also become wider along the build direction. Since there are few new grains introduced, the large columnar grains will only compete with each other; those whose easy-growth directions are better aligned with the local temperature gradient direction \vec{G} will outgrow the less favored grains. This

is a typical competitive growth mechanism [12]. It can be foreseen that as more layers are built only a few grains will win the competition and survive, leading to the large columnar grains in Figure 12a. This grain texture is also observed in the experiments [2, 6, 8]. In Figure 10b ($N_0 = 10^{14}m^{-3}, \Delta T_N = 0K$) and 10c ($N_0 = 10^{15}m^{-3}, \Delta T_N = 5K$), the columnar grains still dominate the grain structure but do not become increasingly wider (and correspondingly the grain size is found to decrease in Table 4). Instead, they are constantly blocked either by new columnar grains (Figure 12b, also experimentally observed in [3]) or a layer of equiaxed grain (Figure 12c, also experimentally observed in [2]). These grain structures can be explained by examining the single-pass grain structures with the same nucleation parameters (in Figure 9a and Figure 8c). In Figure 9a, columnar grains dominate the grain structure with equiaxed grains interspersed among them; when the second layer is built, the top part of the first layer will be re-melted. The interspersed equiaxed grains in the first layer that are partially re-melted will then grow epitaxially to become columnar grains. These “new” columnar grains will join the competitive growth with the existing ones. Since the existing survived grains always have to share the space with the new “competitors”, their growth is limited and the grain size is therefore reduced, as seen in Figure 12b. In Figure 8c, a CET occurs as a thick layer of equiaxed grain at the top of the first layer blocks the epitaxial growth of the columnar grain from the substrate. When the second layer is built, it cannot re-melt the entire layer of equiaxed grains; the equiaxed grains not re-melted are kept as equiaxed, while the partially re-melted ones act as a substrate from which columnar grains grows epitaxially, leading to the “sandwich” structure observed in Figure 12c. When N_0 and $\Delta T_{N,mean}$ favors equiaxed grains the most ($N_0 = 10^{15}m^{-3}, \Delta T_N = 0K$), the equiaxed grain structure is observed in Figure 12d (resembling the experimental observation in [6]), which also has the smallest average grain size and aspect ratio in Table 4.

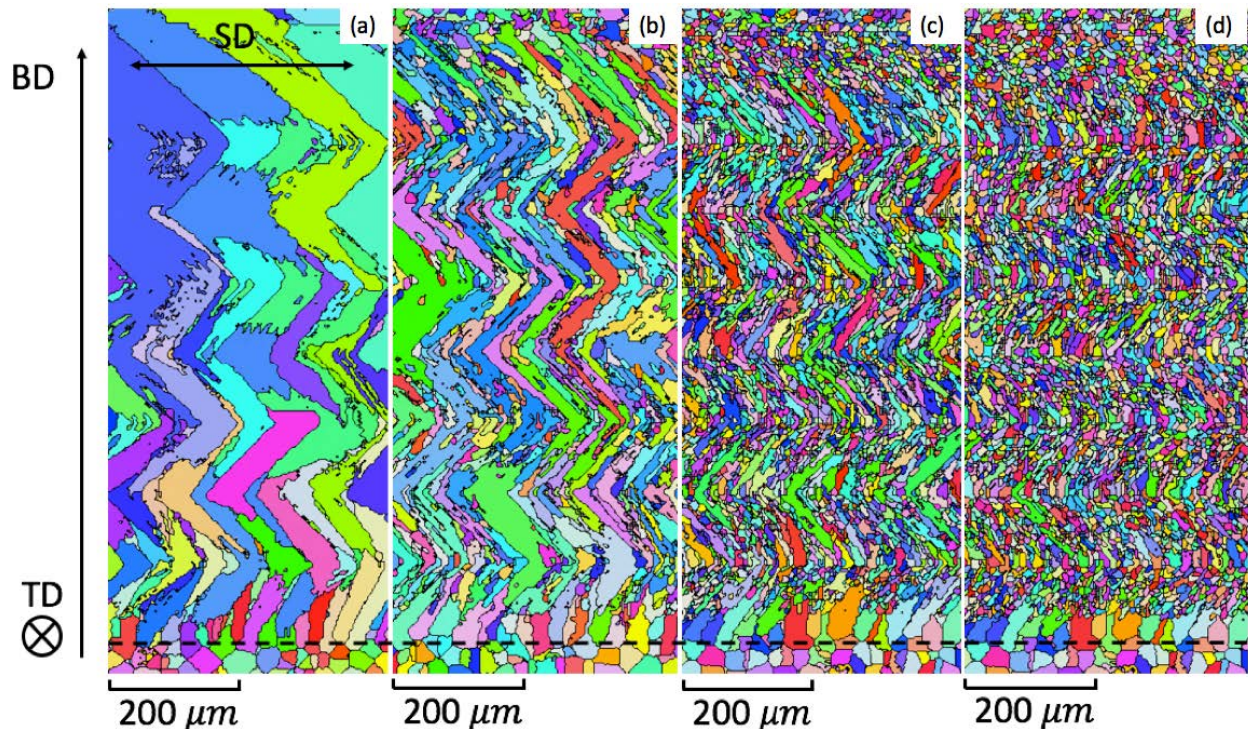


Figure 12: Center plane grain structures obtained with different values of N_0 and $\Delta T_{N,mean}$. (a): $N_0 = 10^{13} m^{-3}$, $\Delta T_N = 10 K$, (b): $N_0 = 10^{14} m^{-3}$, $\Delta T_N = 0 K$, (c): $N_0 = 10^{15} m^{-3}$, $\Delta T_N = 5 K$, and (d): $N_0 = 10^{15} m^{-3}$, $\Delta T_N = 0 K$. The black dashed line indicates the location of fusion line.

Table 4 Average grain size and aspect ratio in Figure 12 and Figure 13.

		average grain size (μm^2)	average aspect ratio
Figure 12	a	24930	2.831
	b	2884	2.621
	c	362	2.239
	d	199	1.859
Figure 13	a	514	1.724
	b	362	2.239
	c	1638	2.17
	d	969	1.92

Up to now the examinations of grain structures have been focused on the center planes of the deposition tracks. However, the 3D grain structures in the deposition tracks are more complex than 2D texture observed on the center planes. Case 3 in Table 3 is chosen to demonstrate the different grain structures on different longitudinal sections. Figure 13a shows a cross section view of grain structure where three longitudinal sections are marked by the black dashed lines denoted by L1, L2, and L3: L1 is the center plane of a track while L2 and L3 are located away from the center plane towards the edge of the track. Figure 13b-d shows the grain structures on these three longitudinal sections.

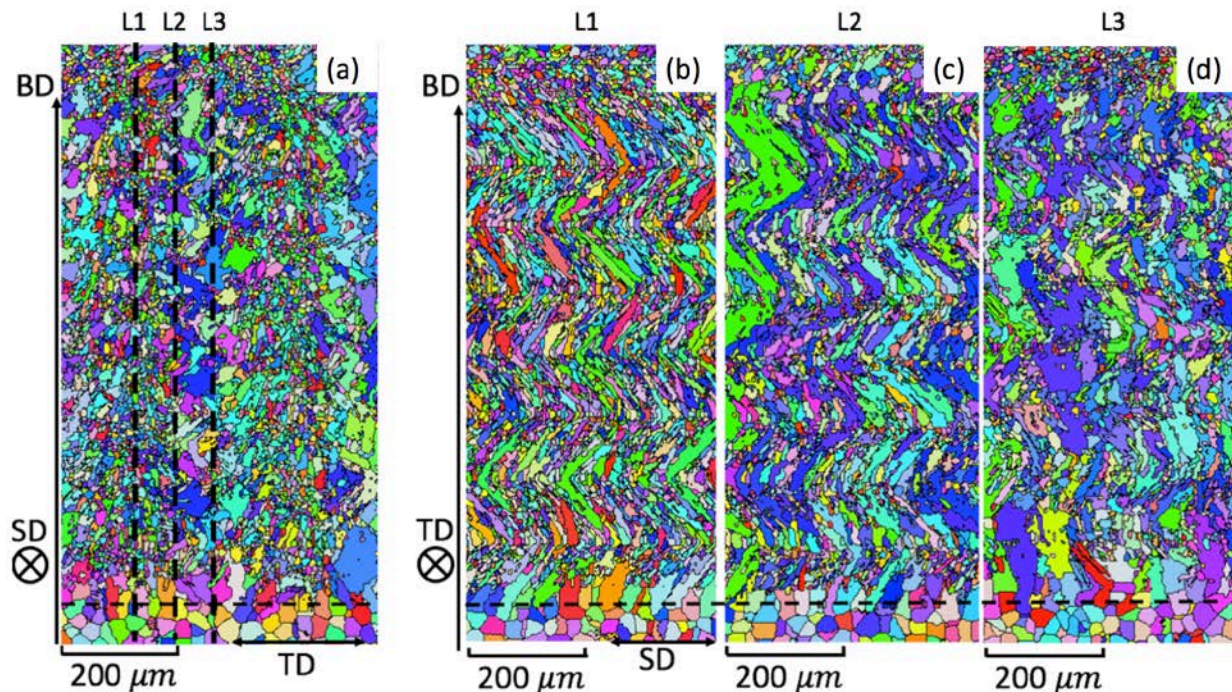


Figure 13: 3D nature of grain structures. (a): the grain structure on the cross section; L1 is the center plane, L2 and L3 are typical longitudinal sections that are away from the center plane. (b) – (d): the grain structures on the L1, L2, and L3. The horizontal black dashed line indicates the location of fusion line.

It is first found on the cross-section (Figure 13a) that smaller and larger grains alternatively show up along the transverse direction (TD); the grains in the track center (where L1 is located)

are smaller than those closer to the track edge (where L2 and L3 are located). And on the longitudinal sections (see Figure 13b-d) the grains size are larger on L2 and L3 than in L1 (also see the average grain size in Table 4). The increase of grain size at L2 and L3 can be attributed to a decrease in the occurrence of equiaxed grains. L2 and L3 are located closer to the edge of the tracks, where G is usually larger and V is usually lower (see Figure 6b and 6c for typical distributions of G and V) and the occurrence of equiaxed grains is discouraged (see Figure 6a). Therefore, less new grains are introduced at L2 and L3, and the existing grains become larger through the competitive growth mechanism. It is also found that the shapes of the grains are different on different longitudinal sections (see Figure 13b-d and the average aspect ratios in Table 4). This can be also attributed to the different grain growth directions in the three longitudinal planes. While all the columnar grains tend to grow along the local temperature gradient \vec{G} , the local \vec{G} is different on the three longitudinal sections: when the laser scans along SD in Figure 13a, the local \vec{G} is aligned very well with SD in L1 and gets increasingly inclined toward the TD in L2 and L3. Therefore, the grains in the three sections stretch along different directions, and the longitudinal sections will cut those grains with different angles with respect to their stretching directions. This causes the grains shapes to be different on the three longitudinal sections. From this demonstration, one can find that analyzing the grain structure simply from one section plane (2-dimensional) can be inadequate to reveal the 3D nature of grain structures.

It can be concluded from this preliminary study that nucleation parameters N_0 and $\Delta T_{N,mean}$ significantly influence the grain structure. Grain structures that are observed in previous experimental works (from columnar-dominated to equiaxed-dominated) are replicated by varying nucleation parameters. It is also demonstrated by simulations that the equiaxed grains can block the growth of columnar grains of the previous layer and become new columnar grains in the next layer (Figure 12b and c). Some discrepancies do exist between the simulated grain structures and experimentally observed ones. The equiaxed grains tend to occur near the molten pool tail in simulations, but Ref. [7] reported that equiaxed grains occurred away from the molten pool tail. Also, fine columnar grains tend to mingle with smaller equiaxed grains (Figure 12b and c) in the simulations, due to the constant nucleation ahead of the SF; but some experimental results can have only the fine columnar grains without too many equiaxed grains visible [7, 35]. These discrepancies can be attributed to multiple reasons such as different thermal history, materials, nucleation conditions and/or mechanisms. Therefore, experimental calibrations and validations about the current model need to be conducted and are considered as important future works.

4. Summary

In this work, the thermal history of a typical MAM process, laser direct deposition, is simulated by a finite volume model, and then cellular automata method combined with a heterogeneous nucleation model is used to simulate the grain structure. Single-pass simulations are first conducted to demonstrate the effects of nucleation parameters, N_0 and $\Delta T_{N,mean}$, and process parameters, P and V_{laser} , on the grain structure. After that, preliminary explorations of the grain structure of a multi-pass multi-layer process are made using different nucleation parameters. The major findings of this work are summarized as follows:

- Larger nucleation density N_0 and smaller critical nucleation undercooling $\Delta T_{N,mean}$ will encourage the heterogeneous nucleation ahead of the solidification front and lead to equiaxed-favored grain structures.
- Laser power P and scanning velocity V_{laser} will significantly influence the temperature gradient G and solidification front velocity V on the fusion surface, which can determine the grain structure being completely columnar, completely equiaxed or mixed with both columnar and equiaxed grains.
- The equiaxed grains can block the growth of columnar grains and also grow to become new columnar grains, leading to complex varying grain structures.
- The grain structures are 3D in nature; they can vary significantly when examined on different planes.
- Important future works include to validate the modeled nucleation and growth mechanisms, as well as to calibrate the nucleation parameters through experiments.

Reference

- [1] W. E. Frazier, "Metal additive manufacturing: a review," *Journal of Materials Engineering and Performance*, vol. 23, no. 6, pp. 1917-1928, 2014.
- [2] L. L. Parimi, G. Ravi, D. Clark, and M. M. Attallah, "Microstructural and texture development in direct laser fabricated IN718," *Materials Characterization*, vol. 89, pp. 102-111, 2014.
- [3] G. Dinda, A. Dasgupta, and J. Mazumder, "Evolution of microstructure in laser deposited Al-11.28% Si alloy," *Surface and Coatings Technology*, vol. 206, no. 8, pp. 2152-2160, 2012.
- [4] V. Ocelík, I. Furár, and J. T. M. De Hosson, "Microstructure and properties of laser clad coatings studied by orientation imaging microscopy," *Acta Materialia*, vol. 58, no. 20, pp. 6763-6772, 2010.
- [5] M. Marya, V. Singh, S. Marya, and J. Y. Hascoet, "Microstructural development and technical challenges in laser additive manufacturing: case study with a 316L industrial part," *Metallurgical and Materials Transactions B*, vol. 46, no. 4, pp. 1654-1665, 2015.
- [6] H. Helmer, A. Bauereiß, R. Singer, and C. Körner, "Grain structure evolution in Inconel 718 during selective electron beam melting," *Materials Science and Engineering: A*, vol. 668, pp. 180-187, 2016.
- [7] L. Thijs, K. Kempen, J.-P. Kruth, and J. Van Humbeeck, "Fine-structured aluminium products with controllable texture by selective laser melting of pre-alloyed AlSi10Mg powder," *Acta Materialia*, vol. 61, no. 5, pp. 1809-1819, 2013.
- [8] T. Niendorf, S. Leuders, A. Riemer, H. A. Richard, T. Tröster, and D. Schwarze, "Highly anisotropic steel processed by selective laser melting," *Metallurgical and Materials Transactions B*, vol. 44, no. 4, pp. 794-796, 2013.
- [9] L. Thijs, M. L. M. Sistiaga, R. Wauthle, Q. Xie, J.-P. Kruth, and J. Van Humbeeck, "Strong morphological and crystallographic texture and resulting yield strength anisotropy in selective laser melted tantalum," *Acta Materialia*, vol. 61, no. 12, pp. 4657-4668, 2013.
- [10] R. Dehoff *et al.*, "Site specific control of crystallographic grain orientation through electron beam additive manufacturing," *Materials Science and Technology*, vol. 31, no. 8, pp. 931-938, 2015.

- [11] P. Collins, D. Brice, P. Samimi, I. Ghamarian, and H. Fraser, "Microstructural control of additively manufactured metallic materials," *Annual Review of Materials Research*, vol. 46, pp. 63-91, 2016.
- [12] S. Kou, *Welding Metallurgy*. John Wiley & Sons, 2003.
- [13] J. Hunt, "Steady state columnar and equiaxed growth of dendrites and eutectic," *Materials Science and Engineering*, vol. 65, no. 1, pp. 75-83, 1984.
- [14] M. Gäumann, C. Bezencon, P. Canalis, and W. Kurz, "Single-crystal laser deposition of superalloys: processing–microstructure maps," *Acta Materialia*, vol. 49, no. 6, pp. 1051-1062, 2001.
- [15] W. Kurz, C. Bezencon, and M. Gäumann, "Columnar to equiaxed transition in solidification processing," *Science and Technology of Advanced Materials*, vol. 2, no. 1, pp. 185-191, 2001.
- [16] A. Zinoviev, O. Zinovieva, V. Ploshikhin, V. Romanova, and R. Balokhonov, "Evolution of grain structure during laser additive manufacturing. Simulation by a cellular automata method," *Materials & Design*, vol. 106, pp. 321-329, 2016.
- [17] J. Zhang, F. Liou, W. Seufzer, and K. Taminger, "A coupled finite element cellular automaton model to predict thermal history and grain morphology of Ti-6Al-4V during direct metal deposition (DMD)," *Additive Manufacturing*, vol. 11, pp. 32-39, 2016.
- [18] A. Rai, H. Helmer, and C. Körner, "Simulation of grain structure evolution during powder bed based additive manufacturing," *Additive Manufacturing*, vol. 13, pp. 124-134, 2017.
- [19] Z. Liu and H. Qi, "Effects of substrate crystallographic orientations on crystal growth and microstructure formation in laser powder deposition of nickel-based superalloy," *Acta Materialia*, vol. 87, pp. 248-258, 2015.
- [20] T. M. Rodgers, J. D. Madison, and V. Tikare, "Simulation of metal additive manufacturing microstructures using kinetic Monte Carlo," *Computational Materials Science*, vol. 135, pp. 78-89, 2017.
- [21] O. Lopez-Botello, U. Martinez-Hernandez, J. Ramírez, C. Pinna, and K. Mumtaz, "Two-dimensional simulation of grain structure growth within selective laser melted AA-2024," *Materials & Design*, vol. 113, pp. 369-376, 2017.
- [22] S. Roy, "Heat transfer modeling of laser cladding process–role of location of injection of powder particles," 2014: International Conference on Heat Transfer, Fluid Mechanics and Thermodynamics.
- [23] S. A. Khairallah, A. T. Anderson, A. Rubenchik, and W. E. King, "Laser powder-bed fusion additive manufacturing: Physics of complex melt flow and formation mechanisms of pores, spatter, and denudation zones," *Acta Materialia*, vol. 108, pp. 36-45, 2016.
- [24] M. J. Matthews, G. Guss, S. A. Khairallah, A. M. Rubenchik, P. J. Depond, and W. E. King, "Denudation of metal powder layers in laser powder bed fusion processes," *Acta Materialia*, vol. 114, pp. 33-42, 2016.
- [25] W. King *et al.*, "Laser powder bed fusion additive manufacturing of metals; physics, computational, and materials challenges," *Applied Physics Reviews*, vol. 2, no. 4, p. 041304, 2015.
- [26] S. Wen and Y. C. Shin, "Modeling of transport phenomena during the coaxial laser direct deposition process," *Journal of Applied Physics*, vol. 108, no. 4, p. 044908, 2010.
- [27] R. Fedkiw and S. Osher, *Level Set Methods and Dynamic Implicit Surfaces*. Springer, 2002.

- [28] W. Tan, S. Wen, N. Bailey, and Y. C. Shin, "Multiscale modeling of transport phenomena and dendritic growth in laser cladding processes," *Metallurgical and Materials Transactions B*, vol. 42, no. 6, pp. 1306-1318, 2011.
- [29] W. Tan and Y. C. Shin, "Multi-scale modeling of solidification and microstructure development in laser keyhole welding process for austenitic stainless steel," *Computational Materials Science*, vol. 98, pp. 446-458, 2015.
- [30] C.-A. Gandin and M. Rappaz, "A 3D cellular automaton algorithm for the prediction of dendritic grain growth," *Acta Materialia*, vol. 45, no. 5, pp. 2187-2195, 1997.
- [31] W. Oldfield, "A quantitative approach to casting solidification: freezing of cast iron," 1966.
- [32] M. Rappaz and C.-A. Gandin, "Probabilistic modelling of microstructure formation in solidification processes," *Acta Metallurgica et Materialia*, vol. 41, no. 2, pp. 345-360, 1993.
- [33] M. Rappaz, C. A. Gandin, J.-L. Desbiolles, and P. Thevoz, "Prediction of grain structures in various solidification processes," *Metallurgical and Materials Transactions A*, vol. 27, no. 3, pp. 695-705, 1996.
- [34] T. T. Roehling *et al.*, "Modulating laser intensity profile ellipticity for microstructural control during metal additive manufacturing," *Acta Materialia*, vol. 128, pp. 197-206, 2017.
- [35] G. Dinda, A. Dasgupta, S. Bhattacharya, H. Natu, B. Dutta, and J. Mazumder, "Microstructural characterization of laser-deposited Al 4047 alloy," *Metallurgical and Materials Transactions A*, vol. 44, no. 5, pp. 2233-2242, 2013.